Lensless Imaging and Sensing

Aydogan Ozcan[1,2,3] and Euan McLeod[4]

[1]Department of Electrical Engineering, [2]Department of Bioengineering, and [3]California NanoSystems Institute, University of California, Los Angeles, California 90095; email: ozcan@ucla.edu

[4]College of Optical Sciences, University of Arizona, Tucson, Arizona 85721; email: euanmc@optics.arizona.edu

Annu. Rev. Biomed. Eng. 2016. 18:77–102

First published online as a Review in Advance on January 25, 2016

The *Annual Review of Biomedical Engineering* is online at bioeng.annualreviews.org

This article's doi: 10.1146/annurev-bioeng-092515-010849

Keywords

microscopy, lab-on-chip, holography, phase recovery, 3D imaging

Abstract

High-resolution optical microscopy has traditionally relied on high-magnification and high–numerical aperture objective lenses. In contrast, lensless microscopy can provide high-resolution images without the use of any focusing lenses, offering the advantages of a large field of view, high resolution, cost-effectiveness, portability, and depth-resolved three-dimensional (3D) imaging. Here we review various approaches to lensless imaging, as well as its applications in biosensing, diagnostics, and cytometry. These approaches include shadow imaging, fluorescence, holography, superresolution 3D imaging, iterative phase recovery, and color imaging. These approaches share a reliance on computational techniques, which are typically necessary to reconstruct meaningful images from the raw data captured by digital image sensors. When these approaches are combined with physical innovations in sample preparation and fabrication, lensless imaging can be used to image and sense cells, viruses, nanoparticles, and biomolecules. We conclude by discussing several ways in which lensless imaging and sensing might develop in the near future.

Contents

1. INTRODUCTION

Historically, bioimaging at the microscopic scale has been performed using lenses, usually the compound microscope and its adaptations (1). Recently, however, imaging without lenses has matured as a modality competitive with traditional lens-based microscopy. In lensless microscopy, a diffraction pattern resulting from an object (based on, e.g., scattering or fluorescence) is recorded directly on a digital image sensor array without being optically imaged or magnified by any lens elements (**Figure 1*a***). This recorded diffraction pattern is then computationally reconstructed to form an "image" of the object. The recent maturation of lensless imaging was made possible largely by the mass production of inexpensive digital image sensors with small pixel size and high pixel counts (2, 3), along with improvements in computing power and reconstruction algorithms used to process the captured diffraction patterns. Here we review recent progress on lensless imaging and sensing in domains including bright-field imaging, cytometry, holography, phase recovery, and fluorescence, as well as the quantitative sensing of specific sample properties derived from such images.

Compared with conventional lens-based microscopy, lensless approaches impart several key advantages: a large space–bandwidth product (large field of view and high resolution simultaneously; see, e.g., **Figure 1*b***), cost-effectiveness, portability (**Figure 1*c*,*d***), and depth-resolved three-dimensional (3D) imaging. These advantages make lensless imaging particularly well suited to analysis applications requiring large statistics. These applications include cytometry "needle-in-a-haystack" diagnostic tasks such as the Papanicolaou smear test for cervical cancer (**Figure 1*b***) (4–7) and blood smear inspection for malaria diagnosis (8, 9), in which the high-resolution inspection of a large number of cells is required because parasitemia is typically less than 1%. Thus, many cells need to be screened to declare a sample "negative" with any reasonable level

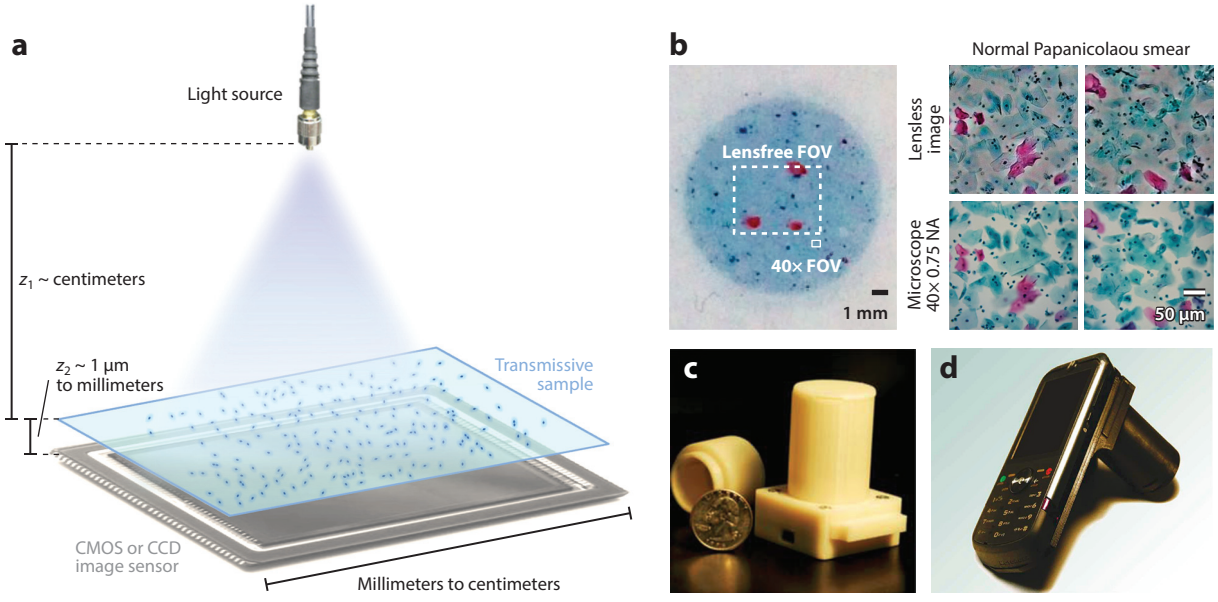

Figure 1

Lensless on-chip imaging. (*a*) General lensless imaging experimental setup based on complementary metal-oxide semiconductor (CMOS) or charge-coupled device (CCD) image sensors. (*b*) Lensless imaging simultaneously provides a large field of view (FOV) and a resolution comparable to that of high-magnification objective lenses. (*c*) Lensless imaging implemented in a compact device where images are transferred via a USB port. (*d*) Lensless imaging incorporated into a camera phone handset. Abbreviation: NA, numerical aperture. Panel *b* modified from Reference 99. Panel *c* modified from Reference 73. Panel *d* modified from Reference 14.

of confidence. More generally, lensless imaging can be a good choice for any type of study that demands statistically significant estimates of a population on the basis of the analysis of a limited sample. Examples include the examination of thousands of sperm trajectories to identify rare types of motion (10, 11) and the performance of a complete blood count (12, 13). Tests designed for samples that have large ranges in number density (concentration) also benefit from imaging approaches with a large space–bandwidth product and depth of field, as it is possible to detect either a few objects or many thousands to millions of objects in a single image. Air quality and water quality tests are two examples of tests in which number density can vary widely.

Other categories of applications that are particularly well suited to lensless imaging are point of care and global health. In an effort to speed up diagnosis and reduce its cost via minimizing reliance on central laboratory testing and diagnostic facilities, these applications demand devices and approaches that are compact, portable, robust, cost-effective, and realistic for widespread distribution. Lensless imaging is a good option for point-of-care and global health applications because it does not require expensive precision microscope objective lenses and light sources. In many instances, individual light-emitting diodes (LEDs) are sufficient for illumination, and the most expensive component in the system is the image sensor, whose cost can be as low as a few tens of dollars due to the mass production of complementary metal-oxide semiconductor (CMOS) image sensors for use in mobile phones (2, 3). Lensless imaging is also compatible with cell phone and smartphone platforms (**Figure 1*d***), which are generally suitable for point-of-care- and global health–related imaging, cytometry, and sensing applications (14–35).

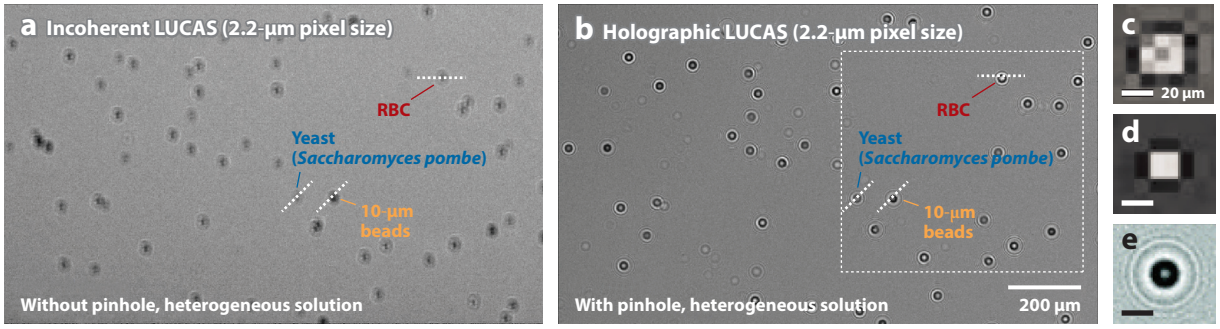

Figure 2

Lensless shadow imaging. (*a*,*b*) Incoherent and coherent shadow images of a heterogeneous solution of particles that consists of red blood cells (RBCs), yeast cells, and 10-μm beads. (*c*–*e*) Images of a 10-μm polystyrene bead. The image scales are identical. (*c*) An incoherent shadow image of a bead acquired at $z_2 = 650$ μm using a sensor with 9-μm pixels. (*d*) An incoherent shadow image of a bead acquired at $z_2 = 300$ μm using a sensor with 9-μm pixels. (*e*) A coherent shadow image of a bead acquired at $z_2 = 625$ μm using a sensor with 2.2-μm pixels. Panels *a*, *b*, and *e* modified from Reference 37. Panels *c* and *d* modified from Reference 39.

2. LENSLESS IMAGING APPROACHES

2.1. Shadow Imaging

The simplest form of lensless imaging is shadow imaging, which requires only the basic hardware setup (**Figure 1*a***) without the need for any image reconstruction procedures. In shadow imaging, a transparent sample is illuminated with a spatially limited light source from a distance of z_1, and the shadow of the sample is recorded directly on the image sensor at a distance of z_2. Due to diffraction over the finite distance z_2 and the relatively large pixel size at the sensor array, the recorded shadows are pixelated, are not in focus, and may consist of either blurry spots when the light source is incoherent (**Figure 2*a*,*c*,*d***) (36) or concentric fringe interference patterns when the light source is coherent (**Figure 2*b*,*e***) (37). The coherence of the light source depends on both the lateral size of the light source relative to z_1 (spatial coherence) and the bandwidth of the spectrum of the light source (temporal coherence) (38). In Section 2.3, we explain how the coherence of the light source can be exploited to reconstruct "images" of the sample. In this section, we rely only on the shadow information, without an attempt to reconstruct images from these undersampled diffraction patterns on the sensor array.

Because typical biological objects of interest are partially transparent, the recorded shadows are not black and white but rather exhibit grayscale complexity. This complexity can be used to identify specific types of particles based on a so-called pattern-matching approach. This approach was initially used to perform blood cell counts to differentiate among red blood cells, fibroblasts, murine embryonic stem cells, hepatocytes, and polystyrene beads of similar sizes (36, 39). Many other types of cells have since been imaged using lensless shadow imaging; these include leukocytes, HeLa cells, sperm cells, A549 cells, RWPE-1 prostate epithelial cells, Madin–Darby canine kidney cells, cardiomyocytes, human alveolar epithelial cells, human mesenchymal stem cells, *Pseudomonas aeruginosa*, *Schizosaccharomyces pombe*, NIH 3T3 cells, MCF-7 cells, bioluminescent *Escherichia coli*, and HepG2 cells (40–53). The lensless imaging approach can monitor cell division, motility, and viability, among other properties (47, 50, 54), and can operate within standard cell culture incubators (**Figure 3**).

For cytometry applications in general, the physical resemblance between the cell morphology and its shadow is not needed, because specific recognition of the cell type is the primary goal.

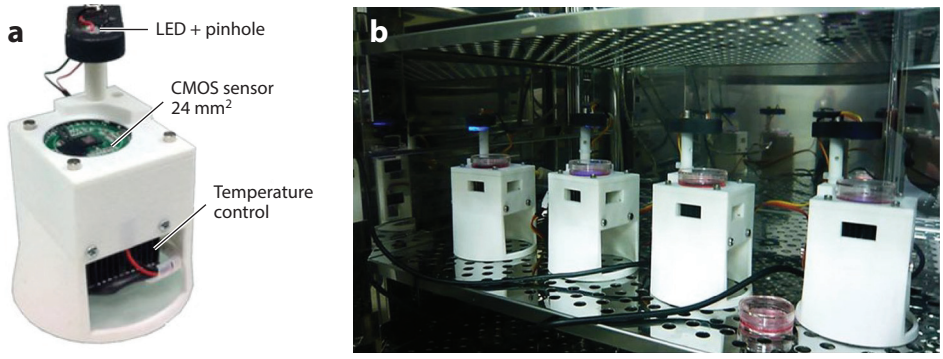

Figure 3

Lensless imaging of live cells within an incubator. (*a*) Compact lensless imaging device with independent temperature control. (*b*) Array of lensless imaging devices operating within a standard incubator. Abbreviations: CMOS, complementary metal-oxide semiconductor; LED, light-emitting diode. Modified from Reference 47.

However, to obtain shadows that bear the closest possible resemblance to the original objects, it is desirable to minimize z_2, thereby minimizing the effect of diffraction (e.g., compare panels *c* and *d* of **Figure 2**). Typically, the smallest practical value of z_2 is determined by the layer of glass placed on the sensor during manufacturing in order to protect it from dust and scratches. The thickness of this protective glass ranges from 10 μm to several hundred micrometers. Even using sensors with sample-to-sensor distances of up to 4 mm, usable shadow information can be obtained for cytometric analysis.

Even if z_2 is minimized by selecting an appropriate sensor-array design, the bottleneck for the resolution of a shadow imaging–based technique will be dictated by the pixel size, which varies between ∼1 μm and ∼10 μm for various CMOS and charge-coupled device (CCD) chips. This undersampling limitation can be improved by placing an array of small apertures directly below the sample. In this configuration, diffraction between the sample and the apertures is minimized, and the intensity of the light transmitted through each aperture can be monitored separately. When the sample is "scanned" relative to the aperture array, assuming that it is a thin sample, the transmittance through each aperture can approximately correspond to the localized transmittance of a single part of the sample at that instant in time. In this way, the aperture array functions similarly to an array of scanning probes, as in the case of, for instance, near-field scanning optical microscopy (NSOM). The resolution of this approach for two-dimensional (2D) objects is limited by the size of the apertures and by the precision with which the sample can be scanned relative to the apertures (which is more typically the practical limiting factor). One way in which the scanning can be performed is through flowing the object(s) of interest along a microfluidic channel fabricated on top of the aperture array, thus forming an "optofluidic" microscope. Such a shadow imaging approach has proven to provide submicrometer resolution of *Caenorhabditis elegans*, *Giardia lamblia*, and other microscale objects (55, 56).

2.2. Fluorescence Imaging

Lensless fluorescence imaging (57, 58) is conceptually similar to shadow imaging, except that (*a*) the scattering-based partially coherent or coherent signal is now replaced with incoherent fluorescent emission from the sample and (*b*) the excitation light and captured emission light are of different wavelengths. The experimental setup thus requires an emission filter to be placed

between the sample and the sensor to reject the excitation wavelength [unless the sensor is not sensitive to the excitation wavelength (59)]. For many fluorescence applications, even with an emission filter, signal-to-background levels are still a concern, and extra measures can be helpful in reducing leakage of excitation light. These measures can include excitation in a total internal reflection geometry (57, 58, 60) or fabrication of specialized CMOS sensor arrays with integrated filters (61–63), where fluorophore densities as small as 100 molecules/μm^2 have been detected.

As with other imaging approaches, the resolution of lensless fluorescence imaging is conventionally limited by the point spread function (PSF) of the system, which is the size of the spot recorded on the image sensor that comes from a single fluorescent point/emitter in the sample plane. Note that this PSF is a strong function of sample height, and one of the limiting factors is diffraction over z_2. As an example, for a typical z_2 value of ~200 μm, the resolution that is dictated by the PSF is ~200 μm (57, 59). This resolution is significantly worse than that of most lens-based microscope systems. Thus, although there are clear advantages in terms of cost, portability, and field of view for a fluorescent lensless imaging setup, the space–bandwidth product obtained using this approach does not initially present a major advantage over that of conventional imaging.

However, it is possible to partially overcome this resolution limitation using hardware and/or computational approaches. One hardware approach, as mentioned above, involves fabricating the filter elements directly into the individual pixels of the sensor array such that z_2 can be minimized, given that no additional filter element is necessary between the sample and the sensor planes. With this approach, a spatial resolution on the order of ~13 μm has been achieved (62). Another hardware approach involves using a tapered faceplate to relay the fluorescence emission (60). In this configuration, a tightly spaced bundle of fibers is placed in contact with the sample. As these fibers relay the light toward the image sensor, the fiber bundle enlarges, providing moderate lensless on-chip magnification. The emission filter can then be placed between the fiber taper and the image sensor. With this setup, the resolution can be as small as 4 μm, determined by the pitch of the fiber-optic taper where it contacts the sample. Yet another hardware approach involves placing a nanostructured mask in close proximity to the object of interest (64, 65). This nanostructured mask generates a PSF that depends on the location of the object/emitter. In other words, instead of the PSF of the system being position independent (i.e., spatially invariant), its shape now depends sensitively on the pattern of nanostructuring that is in close proximity to the fluorescent object plane, allowing the precise locations of nearby objects to be computed from the structure of the recorded emission spot. With this approach, subpixel-level resolutions as good as 2–4 μm have been achieved using compressive decoding (64, 65). Finally, structured excitation can also be used to improve resolution. If the excitation spot is tightly localized and its position is known with high accuracy, then the resolution of the system is limited by the precision with which the excitation spot can be scanned. One way that this technique can be implemented is through the Talbot effect, which has been used to enable fluorescence imaging with a resolution of 1.2 μm on a chip (66). Structured illumination can also be employed to image and perform cytometry through moderately scattering media, such as large volumes of whole blood (13).

Computational methods can be used to further improve the apparent resolution of the image after it has been captured. One of the most common ways to deblur an image is via deconvolution—for example, with the Lucy–Richardson algorithm (57, 67, 68). With this approach, resolutions as good as 40–50 μm have been achieved (57). Even better resolution can be obtained through compressive decoding, which can yield a resolution of ~10 μm (58). This approach relies on the natural sparsity of fluorescent objects and has been used to successfully image fluorescent transgenic *C. elegans* worms (63) in a dual-mode lensfree microscope that merges fluorescence and bright-field modes. A compressive decoding approach has also been used to demultiplex

fluorescence emission channels in samples labeled with multiple colors (69), as well as in the nanostructured on-chip imaging approach discussed in the previous paragraph (65).

2.3. Digital Holographic Reconstruction in Lensless On-Chip Microscopy

As mentioned in Section 2.1, when the aperture of the light source is sufficiently small and monochromatic, the optical field impinging on the sample plane can be considered coherent, and the recorded shadows exhibit interference fringe patterns (**Figure 2*b*,*e***). From these interference fringes, one can infer the optical phase of the scattered light, making it possible to reconstruct the optical field that is transmitted through the objects on the sample and thereby providing an in-focus "image" of the sample (**Figure 4**).

More precisely, the interference fringe pattern recorded on the sensor is an in-line hologram (70, 71), which is the intensity pattern generated by the interference between light scattered from an object on the sample and a reference wave that passes undisturbed through the transparent substrate. At the plane where this light interacts with the sample, we can describe its electric field as the sum of the reference wave at the sample, $E_{R,s}$, and the object wave at the sample, $E_{O,s}$,

$$E_s = E_{R,s} + E_{O,s} = A_R + A_O(x_s, y_s)e^{i\phi_O(x_s, y_s)}, \quad (1)$$

where A_R is the amplitude of the spatially uniform plane reference wave (because $z_1 \gg z_2$, the incident wave can be considered a plane wave over the range between the sample and sensor), $A_O(x_s, y_s)$ is the spatially varying amplitude (transmittance) of the object, and $\phi_O(x_s, y_s)$ is the spatially varying phase (optical thickness) of the object, which is assumed to be a thin sample for the sake of simplicity. The goal of digital holographic reconstruction is to recover A_O and ϕ_O on the basis of measurement(s) of the light intensity further downstream at the image sensor plane.

From these downstream measurements, it is possible to reconstruct the amplitude and phase of the object by using the angular spectrum approach (72). This approach consists of computing the Fourier transform of the captured hologram, multiplying it by the transfer function of free space, and then inverse Fourier transforming. Mathematically,

$$E_r = \mathcal{F}^{-1}\{\mathcal{F}\{E_i(x, y)\}H_{z_2}(f_x, f_y)\}, \quad (2)$$

where E_r is the reconstructed optical field of the object, $E_i(x, y)$ is the captured hologram, and $H_{z_2}(f_x, f_y)$ is the transfer function of free space ($n = 1$):

$$H_{z_2}(f_x, f_y) = \begin{cases} e^{ikz_2\sqrt{1-\left(\frac{2\pi f_x}{k}\right)^2-\left(\frac{2\pi f_y}{k}\right)^2}}, & f_x^2 + f_y^2 < \frac{1}{\lambda^2} \\ 0, & f_x^2 + f_y^2 \geq \frac{1}{\lambda^2} \end{cases}. \quad (3)$$

Here, λ is the wavelength of the light, $k = 2\pi/\lambda$, f_x and f_y are spatial frequencies, and z_2 is the same sample-to-sensor distance shown in **Figure 1*a***. Often z_2 may not be precisely known before the capture of the hologram, and some computational "refocusing" can be performed to estimate it and provide the sharpest reconstructions.

In contrast to the shadow imaging presented in Section 2.1, two of the significant advantages of digital holographic reconstruction are the improvements in resolution and detection signal-to-noise ratio (SNR) (73). These improvements are visible in **Figure 4**, where grating objects cannot be directly resolved from the raw shadows but are visible upon holographic reconstruction. This resolution improvement helps not only in discerning two nearby objects, such as lines on a grating, but also in imaging finer features on a single object (see, e.g., **Figure 4*f*,*g***).

There are also some limitations to the method of this basic implementation of digital holographic reconstruction, although many of these limitations may be overcome or mitigated through

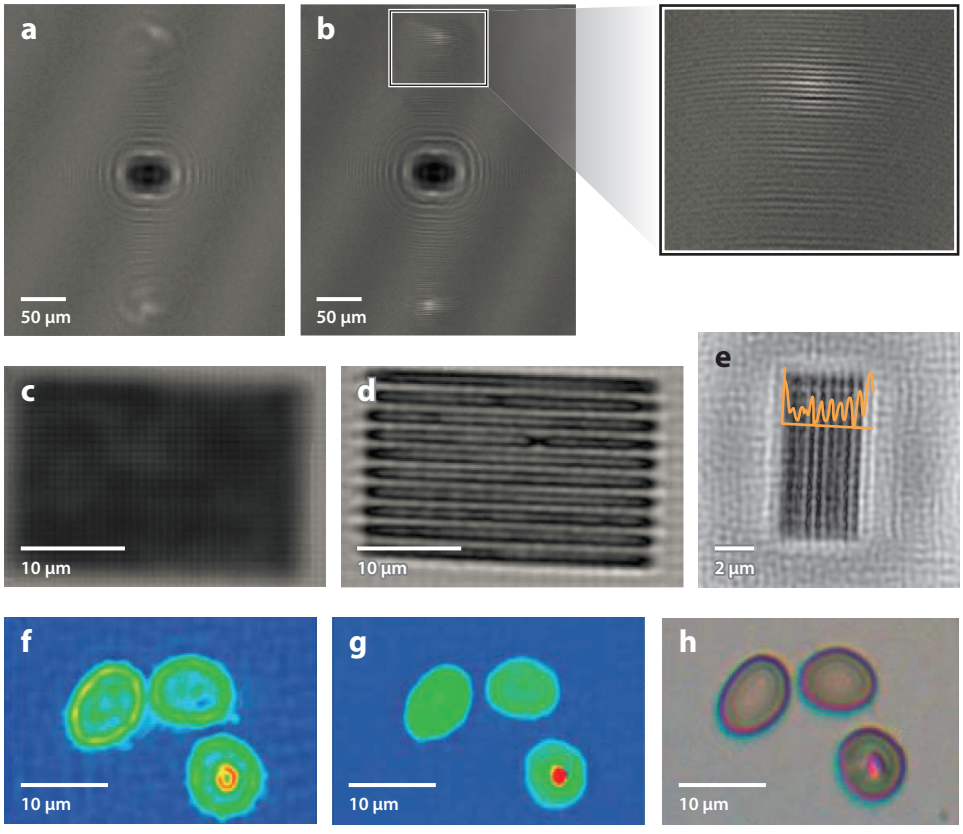

Figure 4

Digital holographic lensless imaging. (*a*) Raw hologram image of a grating with 1-µm half-pitch. (*b*) Pixel-superresolved hologram of the same grating. (*Inset*) Holographic fringes corresponding to high spatial frequencies become visible in the superresolved hologram. (*c*) Reconstruction of the amplitude transmittance from the low-resolution hologram in panel *a*. The grating lines are not resolved. (*d*) Reconstruction of the amplitude transmittance from the superresolved hologram in panel *b*. The grating lines are now resolved. (*e*) Reconstruction of the amplitude transmittance (*orange*) of a different grating with 225-nm half-pitch, demonstrating the ability of lensless imaging to resolve extremely fine features. (*f*) Lensless amplitude image of red blood cells, one of which is infected with a malaria parasite (*Plasmodium falciparum*). (*g*) Lensless phase image corresponding to panel *f*, where the malaria parasite appears more distinctly. (*h*) Conventional 40× objective microscope image. Panels *a–d* modified from Reference 80. Panel *e* modified from Reference 82. Panels *f–h* modified from Reference 8.

alternative approaches presented throughout the rest of Section 2. One constraint is that the resolution is limited by the pixel size of the sensor, which is ~1–2 µm for current mass-produced sensors. Methods to overcome this limitation are discussed in Section 2.4. A second limitation is the presence of a twin-image artifact that is a consequence of only being able to measure the intensity of the field at the image sensor plane. Overcoming this limitation is discussed in Section 2.6. Third, it is necessary that the scattered wave be weak compared with the reference wave, which restricts this simple form of holographic reconstruction to relatively sparse samples. However, this limitation has also been overcome, as discussed further in Section 2.6. Fourth, the requirement of coherence between the illumination wave and the scattered wave means that it is not immediately

possible to combine this approach with fluorescence, unless some changes are made to the experimental setup. Finally, color imaging is not trivial due to the temporal coherence requirement that the light source be monochromatic; this topic is addressed in Section 2.7 with several approaches that can provide color information in holographically reconstructed lensfree images.

2.4. From Pixel-Limited Resolution to Signal-to-Noise Ratio–Limited Resolution

In a conventional microscope, the resolution is typically limited by the numerical aperture (NA) of the objective lens following the expression $\Delta x \sim \lambda/(2\text{NA})$. Without immersion media, it is not possible to utilize lenses with NA > 1. This limiting value of NA results in the oft-quoted conventional diffraction limit of $\Delta x > \lambda/2$.

In holographic lensless on-chip imaging, the resolution of the computationally reconstructed image is equal to the resolution of the captured hologram. Because there is no lens with finite NA to limit the resolution, the resolution-limiting factor is, in theory, the refractive index (n) of the medium that fills in the space between the sample and sensor planes and, in practice, the pixel size of the sensor. The drive to miniaturize image sensors for use in mobile phones has helped reduce the pixel size on manufactured sensors; however, the smallest commercially available pixel sizes are still larger than 1 μm. This native pixel size would result in resolutions comparable to conventional microscope objectives, with NA ∼ 0.25 for 500-nm light. Although this resolution can be sufficient for many applications, there has recently been a strong push to improve the resolution of lensless imaging beyond this limit so as to extend the range of applications and capabilities of on-chip microscopy tools.

Assuming a sensor could have arbitrarily small pixels, there would still be a diffraction-imposed limit on the resolution of the captured hologram. Because z_2 is larger than several wavelengths, disturbances in the electric field with spatial frequency components greater than $1/\lambda$ resulting from fine spatial features in the object will evanescently decay, whereas only those disturbances with characteristic size greater than approximately $\lambda/2$ will propagate to the far field (as shown mathematically in Equation 3). Note, however, that although these spatial frequencies decay, they are not lost completely. Furthermore, from the knowledge that the electric field must physically be described as a continuous function, it is theoretically possible, at least for a space-limited object, to recover these "lost" spatial frequencies through analytic continuation (74, 75). In practice, the success of these approaches depends on the measurement's SNR and object support information; therefore, they have been limited in their use.

Additionally, the temporal and spatial coherence properties of the light source can independently limit the resolution of lensless holographic imaging. The coherence of the system determines the maximum angle at which light scattered from an object will produce an observable interference pattern at the detector (38). This maximum scattering angle corresponds to the NA of this lensless imaging system and its half-pitch resolution:

$$\Delta x = \frac{\lambda}{2\,\text{NA}} = \frac{\lambda}{2n\sin\theta_{\max}}. \tag{4}$$

The maximum scattering angle ($\theta_{\max}$) may be limited by the temporal and/or spatial coherence of the system. The temporal coherence is determined primarily by the spectral bandwidth of the system λ, which implies the following coherence length (38):

$$L_{\text{coh}} = \left(\frac{2\ln 2}{\pi}\right)\frac{\lambda^2}{n\Delta\lambda}. \tag{5}$$

A coherent interference pattern is generated when the phase delay between a reference ray and a scattered ray is no longer than the coherence length, implying

$$\theta_{\max} \leq \arccos\left(\frac{z_2}{z_2 + L_{\text{coh}}}\right). \tag{6}$$

Substituting this expression into Equation 4 yields the limit to the resolution imposed by temporal coherence of illumination.

The spatial coherence is influenced primarily by the lateral size of the light source D and the source-to-sample distance z_1, assuming $z_1 \gg z_2$, as is the case for an on-chip imaging design. The resulting maximum scattering angle is given by

$$\theta_{\max} \leq \arctan\left(\frac{0.61\lambda z_1 / D}{z_2}\right), \tag{7}$$

where the numerator of the arctangent is one-half the distance to the first zero of the complex coherence factor of the light source, observed at the sample plane (38). When substituted into Equation 4, this value provides the spatial coherence imposed limit on resolution.

Taken together, the above equations can be used to prescribe the necessary properties of the light source to achieve a desired resolution. For example, if we ignore the pixel size–induced undersampling and resolution limitation (addressed in the following paragraphs) to achieve a resolution equivalent to that from a 0.8-NA microscope objective using 500-nm light in air with $z_2 = 100$ μm, the spectral bandwidth of the source must be $\Delta\lambda < 1.6$ nm, and the ratio D/z_1 must be $<2.2\times10^{-3}$. These levels of coherence do not require a laser source and can be attained through the combination of an LED, a narrowband interference filter, and a large-diameter pinhole or multimode optical fiber with z_1 on the order of a few centimeters. Exceedingly coherent sources, such as lasers, can ultimately degrade image quality through speckle artifacts or spurious interference fringes resulting from multiple reflections within and by the substrate (76).

Even with a coherent or partially coherent light source, there still remains a "resolution gap" between the sensor pixel size of ~1 μm and the "diffraction limit" of $\lambda/2$. One particularly successful approach to bridge this gap is pixel superresolution. In this technique, multiple captured images of the same object that are shifted with respect to each other in the x and y directions by noninteger numbers of pixels can be synthesized into a single high-resolution image. This technique enables many images with large pixel sizes to be converted into an image with much smaller virtual pixels. Note that this approach is not simply interpolation, or upsampling, which can never truly improve resolution; rather, it allows one to recover fine features that are normally undersampled. The first step of this procedure involves estimating the shifts between the images with subpixel accuracy. This step can be done using a variety of "optical flow" techniques, such as iterative gradient-based techniques (77, 78). Next, the raw images are upsampled to the desired new high resolution; the intermediate values are initially determined through interpolation of neighboring low-resolution pixels. One way of computing the pixel-superresolved image, termed the shift-and-add method, is as follows (79):

$$\hat{\boldsymbol{z}} = \left(\sum_{k=1}^{N} F_k^T D^T D F_k\right)^{-1} \left(\sum_{k=1}^{N} F_k^T D^T \boldsymbol{y}_k\right). \tag{8}$$

Here, the F_k are block-circulant matrices that describe the relative shifts between the images, D is the decimation (downsampling) operator that converts a high-resolution image to a low-resolution image, and the $\boldsymbol{y}_k$ are the captured images, represented (reshaped) as a column vector. The high-resolution estimate $\hat{\boldsymbol{z}}$ is likewise represented as a column vector. In this equation, the second term is conceptually the sum of the shifted raw images, whereas the first term is a normalization parameter

based on the number of shifted images, their degree of redundancy, and the desired amount of resolution enhancement. In addition to this shift-and-add method of pixel superresolution, other methods exist, such as iterative gradient-descent optimization routines (77).

Whereas these equations are written with shifts of the image sensor in mind, it is often more practical to shift the light source rather than the object (80), although a flowing object within a microfluidic channel can also be used (81). This is because larger and less-precise shifts of the light source can be used to generate subpixel shifts on the image sensor due to the large z_1/z_2 ratio. This approach can also be implemented in field-portable devices where, instead of a single light source being shifted, multiple, spatially separated light sources are sequentially activated (8).

Pixel superresolution has been successfully combined with lensless holographic on-chip microscopy to obtain half-pitch resolutions as fine as 225 nm on commercially available CMOS sensors with a pixel size of 1.12 μm (**Figure 4*e***) (82, 83). In this approach, a high-resolution hologram (e.g., that in **Figure 4*b***) is synthesized using pixel superresolution before the image is computationally reconstructed. Because the resolution of the reconstruction equals the resolution of the hologram, the capture of fine spatial features in the hologram allows fine features on the object to be recovered. With this approach, lensless holographic imaging has been made nearly diffraction limited, with half-pitch resolutions equivalent to those from 0.8–0.9-NA microscope objectives (82, 84).

Although pixel superresolution has enabled high-resolution imaging in combination with small-pixel CMOS sensors, its value is even more apparent when combined with large-pixel CCD sensors. CCD sensors are typically lower noise and can have larger pixel counts than CMOS sensors; however, their pixel sizes are often greater than ∼4–5 μm, which limits their resolution when used as a lensless imaging device (**Figure 2*c*,*d***). Through the use of pixel superresolution in combination with CCD sensors, half-pitch resolutions as fine as 0.84 μm have been achieved (82). This technique generates gigapixel images with more than one billion pixels that carry useful (i.e., resolvable) information. In other words, the smallest resolvable feature and the characteristic linear dimension of the field of view differ by more than four orders of magnitude.

The performance of pixel superresolution can be further improved if the spatial responsivity of each pixel is known at a microscopic scale. This is known as the pixel function, which is not uniform because of the presence of, for instance, wiring and microscopic circuit elements present at each pixel and the potential for a microlens to be fabricated on top of each pixel. Several approaches can be used to determine the pixel function of a sensor a posteriori. One method is to scan a tightly focused laser beam across a pixel and record its response. This method is reasonable for larger-size pixels such as those on CCD sensors (82). However, for ∼1-μm pixels, the diffraction-limited spot size of the laser beam is approximately equal to that of the pixel size, and useful information cannot be obtained unless a near-field scanning probe is utilized. In cases where experimental measurements of the pixel function become difficult, one can employ alternative computational approaches based on blind deconvolution routines or optimization routines (82). Here, a known object with fine features is holographically imaged and reconstructed with an initial guess for the pixel function (e.g., a guess that the pixel function is uniform across the pixel). Then the guess for the pixel function is modified iteratively. Modifications that lead to an improvement in the reconstruction quality are pursued until convergence is achieved. As an example, this approach was used in the reconstruction of **Figure 4*e***.

In addition to the holographic lensless imaging approach, subpixel resolving techniques have been used in other lensless imaging approaches. In lensless microscopes based on near-contact-mode imaging, pixel superresolution techniques have been used to achieve 0.75-μm resolution of objects carried by the microfluidic flow (85). This approach can be combined with machine learning to discriminate between different types of cells (86). A similar contact imaging approach,

termed ePetri, has recently been used to image static samples in near contact with the image sensor. Here, a shifting light source creates shadows that shift over fixed pixel locations (87, 88). The ePetri platform has been applied to the imaging of viral plaques (89) and waterborne parasites (90).

2.5. Three-Dimensional Lensless Imaging

Another advantage of the holographic lensless imaging approach is the ease with which images at different depths can be computationally generated through variation of the value of z_2 in Equation 2. This can be considered digital refocusing of a captured image. With this approach, it is possible to obtain some degree of 3D sectioning. Here, the depth of focus of a single object scales with O^2/λ, where O is the object diameter. Practically, unless other 3D imaging techniques are utilized, the depth of focus results in an axial resolution of at least ~40 μm (91–93). The typical range of depths of digital refocusing is on the order of millimeters. It is important to realize that with this simple approach, the sample must remain relatively sparse so that a clean reference wave is still available for holographic reconstruction.

Improved localization in z of sparse objects is possible through triangulation using at least two light sources: one that illuminates the sample at normal incidence and another that illuminates the sample at oblique incidence (94). With this approach, localization accuracies of ~300–400 nm have been achieved (94). Additionally, for unique computational reconstructions of the recorded holograms, it is helpful if two different wavelengths (e.g., blue and red) are used for the two illuminations so that it is unambiguous which hologram comes from which light source. This technique has been successfully used to track and finely resolve the 3D trajectories of thousands of sperms in a volume of ~5.0 mm × 3.5 mm × 0.5 mm in a single experiment (10, 11). This large number of statistics has been instrumental in identifying rare and unique swimming patterns in human and animal sperm, such as the finding that of the human sperm that travel in helical paths in vitro, ~90% travel in a right-handed helix as opposed to a left-handed helix.

When many light sources are used sequentially from many different angles, lensless tomographic microscopy can also be performed. Here, many holograms are recorded from significantly different angles. A single tomogram can be reconstructed from these multiple holograms via, for instance, filtered back-projection (91, 95). This approach has also been implemented in a compact portable platform (96), used to image *C. elegans* worms in three dimensions without the use of lenses (91, 97), and combined with a microfluidic device for imaging flowing samples, demonstrating the first implementation of an optofluidic tomographic microscope (98).

2.6. Reconstruction of Dense Images Using Iterative Phase Recovery: Solutions for Phase Recovery Stagnation in Lensless On-Chip Microscopy

In the preceding sections, the coherent interference pattern captured on the sensor was regarded as an inline hologram—that is, the interference between a reference beam and a scattered object beam. This assumption enables one to infer the optical phase of the light wave (although this phase also includes a twin-image artifact), which is at the core of the computational reconstruction of an image of the object. However, this coherent interference pattern can more generally be considered a coherent diffraction pattern. Under this more general consideration, where a clean reference wave is not necessarily present, the optical phase can no longer be inferred from a single measurement. However, with additional information—for example, either from a priori knowledge of the nature or size of the object (73) or from multiple measurements at different z_2 distances (4, 5, 99)—it becomes possible to recover the lost phase information, which eliminates the source of the

twin-image artifact and enables the high-fidelity reconstruction of dense connected samples, such as tissue samples used in clinical examination in pathology labs.

For samples that are still relatively sparse, the optical phase (without the twin-image artifact) can be recovered through the assumption that outside the boundaries of individual objects, the amplitude and phase of the light should be uniform. This additional boundary information regarding the sample is enough to enable the elimination of the twin-image artifact. One way to remove this artifact is to computationally propagate the optical field back and forth between the sensor (hologram) plane and the sample plane, enforcing known information at each plane (73). At the sensor plane, the known information is the captured amplitude of the optical field, whereas at the sample plane, the known information is the optical field outside the rough boundaries of the objects. After each propagation, components of the optical field corresponding to known information are replaced with that information, while the remaining components continue to be dynamically updated with each propagation. Experiments have shown that after several iterations of this procedure, the optical field converges to a physically consistent function, and it is possible to reconstruct the objects with minimal twin-image artifacts. A key parameter in the success of this approach is the ability to accurately define the boundaries of objects in the image (known as the object support). In practice, it can sometimes be a challenge to accurately define these regions in an automated fashion. Lens-based reflective imaging of the same sample has also been used to improve the selection of the object support in a lensless on-chip microscope (100).

The iterative phase recovery algorithm described above is only one example of the whole class of phase recovery algorithms, dating back to the Gerchberg–Saxton algorithm, which was pioneered in the 1970s (101, 102). In general, these algorithms involve computationally propagating an optical field between planes and enforcing any known information at each plane. These approaches can involve more than two planes, and the known information can take many different forms. A specific type of phase recovery approach that has shown widespread success is based on multiple amplitude or intensity measurements at various values of z_2 (4, 5, 99). This technique can be used to image dense, connected samples such as tissue slices (99) or blood vessel formation within engineered tissue models (103), which would not normally be recoverable using on-chip holography alone. Here, iterative propagation among the various planes is performed, enforcing the measured amplitude of the optical field at each plane. Once convergence is achieved, the optical field of any given measurement plane can be propagated to the sample plane to generate amplitude and phase images of the object. Because this approach does not rely on the presence of a clean reference wave, it works well even for dense, connected samples without the need for any object support information (**Figure 5**).

In these iterative phase recovery algorithms, several iterations are often required to achieve a desired level of convergence, which can take considerable computational time. One way to speed up convergence and computational time is through the transport-of-intensity equation (104, 105):

$$\frac{\partial I(x,y)}{\partial z} = -\frac{\lambda}{2\pi}\nabla_{\perp}\cdot[I(x,y)\nabla_{\perp}\phi(x,y)], \tag{9}$$

where $I(x, y)$ is the intensity of the optical field, $\nabla_{\perp}$ is the gradient operator in the (x, y) plane, and ϕ is the optical phase. This equation serves as an alternative to, for instance, the coherent Rayleigh–Sommerfeld diffraction integral, which is often used to calculate the propagation of an optical field. Using the measured intensities at different planes as boundary conditions, one can numerically solve this partial differential equation to provide an estimate for the optical phase. With the transport-of-intensity equation, the computational time to convergence can be sped up considerably (99), and the quality of the reconstructed image remains high.

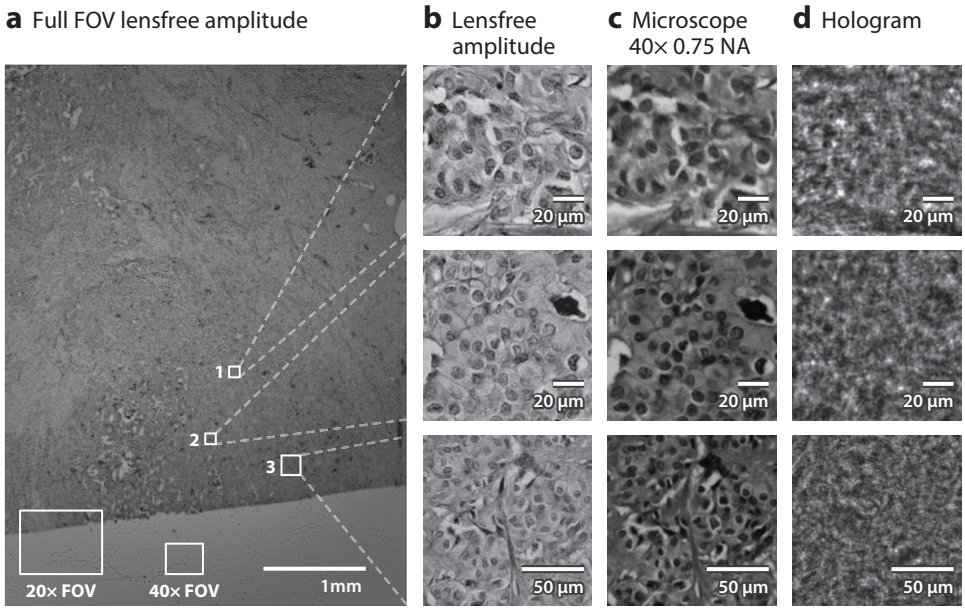

Figure 5

Tissue imaging using multiheight phase recovery. (*a*) Full field-of-view (FOV) amplitude image of a stained human breast carcinoma tissue slice, reconstructed from measurements of diffracted intensity at different sample-to-sensor distances. (*b*) Magnified regions of interest from panel *a* clearly showing individual cells and their nuclei. (*c*) Comparison images of the same regions using a conventional bright-field microscope. (*d*) Examples of some of the raw diffracted intensities captured by the sensor. Abbreviation: NA, numerical aperture. Modified from Reference 99.

Another holographic on-chip microscopy approach to imaging of dense samples is lensfree imaging using synthetic aperture (LISA) (106). The experimental setup for LISA is similar to that used in lensless tomography; however, the samples in LISA are assumed to be 2D (as in a histopathology sample), and the processing algorithm is entirely different. By illuminating the sample at high angles of incidence, one can convert high spatial frequencies at the object to lower spatial frequencies (and vice versa) at the hologram (image sensor) plane. High-resolution reconstructions with an effective NA of 1.4 can be obtained by cycling through a sufficient number of incidence angles and orientations (together with source-shifting- or sample-shifting-based pixel superresolution), thus sampling a large region in the frequency domain. Furthermore, if there is some overlap (redundancy) between the images in the frequency domain, these separate measurements can be used to perform iterative phase recovery, enabling the imaging of dense samples (**Figure 6**).

2.7. Color Imaging in Lensless On-Chip Microscopy

The high-resolution imaging techniques described in Sections 2.3–2.6 all rely on the capture of coherent interference patterns on the sensor. When the illumination is incoherent, as discussed in Sections 2.1 and 2.2, the resolution is relatively poor. To obtain coherence in illumination, the light must be monochromatic. This requirement results in monochrome images, which can be less desirable from the point of view of, for instance, microscopists, pathologists, and medical practitioners. In many cases, valuable information is encoded in color from specific stains applied

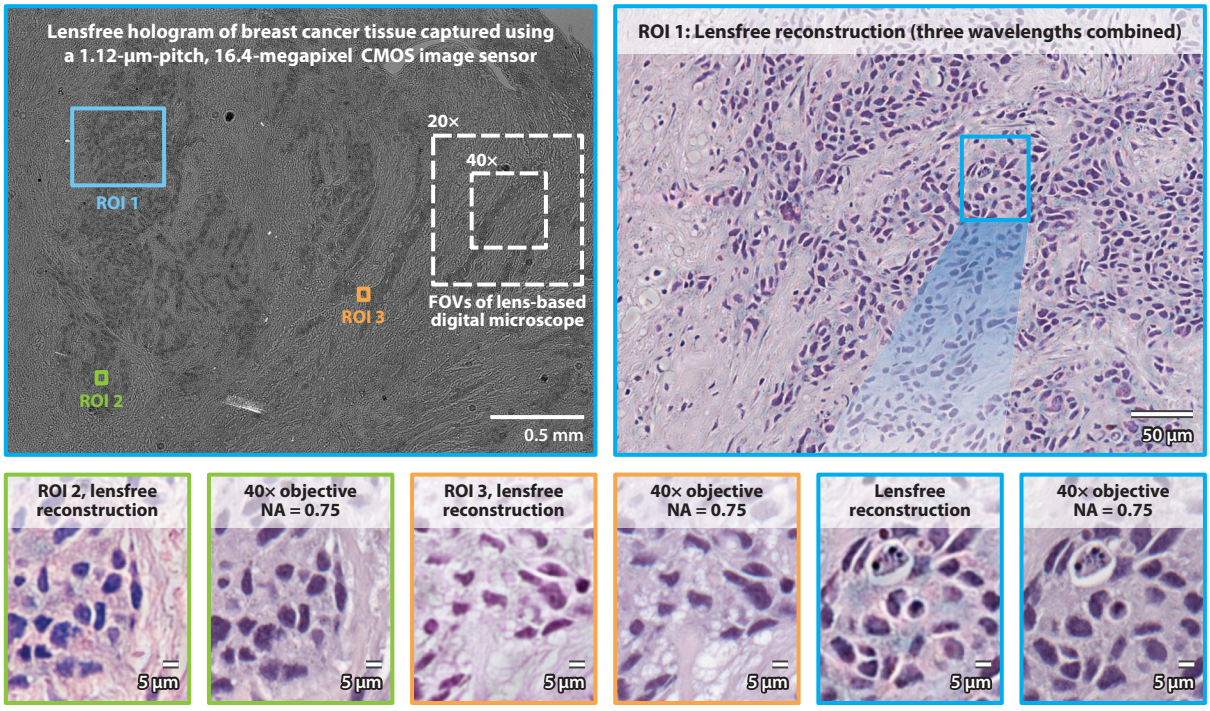

Figure 6

Tissue imaging using a lensfree synthetic aperture approach. The top left panel shows the captured raw hologram from a stained human breast cancer tissue for the full field of view (FOV) of the lensless imaging system. The other panels show magnified regions after reconstruction and colorization. Abbreviations: CMOS, complementary metal-oxide semiconductor; ROI, region of interest. Modified from Reference 106.

to biological samples, and even when the color information does not provide added information, it is nonetheless desirable so that practitioners trained to make diagnoses on the basis of conventional microscope images are easily able to transition to lensless images without the need for retraining. In these cases, a statistical color mapping from intensity to a precalibrated color map may be sufficient, yielding quite comparable results against a traditional lens-based color microscope (99).

Another relatively straightforward coloring approach involves first capturing three images sequentially with monochromatic red, green, and blue light sources, then digitally superimposing the resulting reconstructions (107). This approach is successful in recovering the color of the object (**Figure 7*a***); however, it also leads to undesirable "rainbow" artifacts around the objects, which are a consequence of twin-image artifacts. Some of these rainbow artifacts can be mitigated by performing color averaging in the YUV color space (**Figure 7*b***), where the Y channel represents brightness information and the U and V channels represent color information (6). In this approach, a monochromatic, high-resolution image is first obtained using, for example, pixel superresolution, which defines the Y channel. The color information (UV channels) is then obtained by acquiring three lower-resolution images using red, green, and blue illumination, which are initially combined into RGB color space and then converted to the YUV color space. The U and V channels of the resulting lower-resolution image are subsequently averaged with a spatial window (e.g., ~10 μm) that is used to mitigate the rainbow artifact, while the Y channel is replaced with the pixel superresolved image. In the last step, the resulting "hybrid" YUV image is converted back into an RGB image of

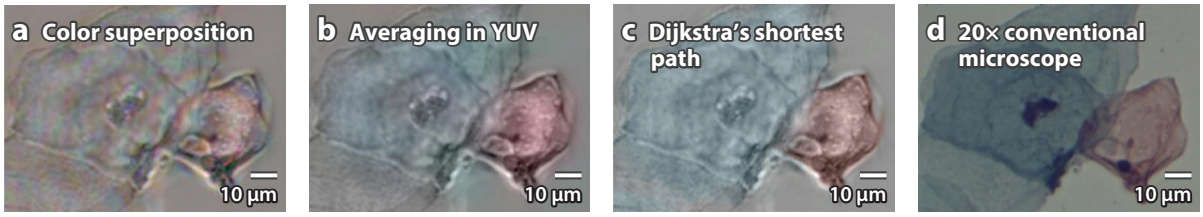

Figure 7

Lensless color imaging methods. Each panel shows an image of two cells in a stained Papanicolaou smear. (*a*) The direct superposition of reconstructions from multiple color channels results in washed-out colors and rainbow-like artifacts. (*b*) Averaging image colors in the YUV color space can mitigate the rainbow artifacts. (*c*) Colorizing the image using Dijkstra's shortest path method also mitigates rainbow artifacts; however, slight color variations within a single object are lost. (*d*) A comparison image acquired using a conventional 20× microscope objective is used as the gold standard for color imaging. Modified from Reference 6.

the sample. Another way to overcome these rainbow artifacts is Dijkstra's shortest path algorithm, which is a graph-search algorithm aiming to find the shortest path from a given node to the remaining nodes. This approach has also been used for lensfree color imaging, yielding very similar results to those of the YUV color-space averaging approach discussed above (**Figure 7*c***) (6, 108).

These color imaging approaches, among others, have been implemented in a variety of portable devices. Both YUV averaging and Dijkstra's shortest path method have been successfully incorporated into a portable pixel superresolution–based on-chip microscopy device using different-colored LEDs (7). In shadow imaging, color imaging has been used to evaluate hemoglobin concentrations (109) and enzyme-linked immunosorbent assays (110). In the optofluidic microscope approach, in both a format where the object flows over small apertures and a format where the object flows without apertures but in close proximity to the image sensor (see Sections 2.1 and 2.4), color imaging has been performed, again using multiple LEDs (41, 111, 112). Color imaging has also been incorporated with the lensfree tomography approaches discussed in Section 2.5 (113).

3. LENSLESS SENSING

The lensfree computational imaging devices described above can also be converted into sensors when combined with specialized substrates or specialized photonic elements and automated image processing routines. In this section, we describe some examples of lensless sensing, including the fabrication and imaging of self-assembled nanolenses for the sensing of nanoscale particles and viruses, measurements of cellular mechanics, the use of metallic beads as labels for biochemical specificity, and sensing based on plasmonics.

3.1. Self-Assembled Nanolenses for Detection of Nanoparticles and Viruses over Large Fields of View

An ever-present challenge in biosensing and imaging is the ability to detect smaller and smaller objects (114, 115). The lensless imaging approaches described in Section 2 are well able to detect and image microscale objects such as single cells; however, the detection of nanoscale objects such as single viruses or nanoparticles is difficult. The primary reason is that the intensity of the electromagnetic wave scattered by such small particles is so weak compared with the background (reference) wave intensity that it can become lost in the background noise of these on-chip imaging systems. Indeed, individual spherical particles smaller than ~250 nm cannot be reliably discerned

from background noise via the above-discussed approaches, unless a significant refractive index contrast exists between the particle and the surrounding medium.

In order to reduce this detection limit to permit the sensing of virus-scale particles, a self-assembly approach has been used to fabricate liquid polymer nanoscale lenses around the target particles. These self-assembled nanolenses provide an increased scattering signal compared with the particles alone, partially due to the increased volume and partially due to their refractive geometry preferentially directing the scattered signal toward the image sensor. Three distinct approaches have been pursued to form these nanolenses, namely tilting-based formation (83, 116, 117), formation by solvent evaporation (118, 119), and formation by the condensation of a polymer vapor (120, 121).

In the tilting-based approach, the target nanoparticles are suspended in a Tris-PEG-HCl buffer. A drop of this suspension is placed on a plasma-treated glass surface and left to rest for a few minutes, after which the surface is gently tilted to let the bulk of the drop slide to the edge of the glass. In the wake of the drop, small droplets (nanolenses) of liquid are pinned around target particles that adhere to the glass. In this liquid, polyethylene glycol (PEG) is the critical component. PEG is a nontoxic water-soluble polymer, and at the molecular weight used here (600 Da), it evaporates very slowly in ambient conditions. This last property allows nanometer-scale droplets of PEG to remain stable for many minutes to hours, permitting the acquisition of multiple images. With this approach, nanoparticles and viruses with diameters as small as 100 nm can be sensed over large fields of view (e.g., 20–30 mm^2) by use of lensless on-chip imaging (**Figure 8*a–d***) (117).

Another approach to nanolens formation involves letting the initial drop evaporate instead of tilting it to the side. In this approach, the particles are again suspended in a liquid mixture. This mixture contains PEG, surfactant, and a volatile solvent. The volatile solvent evaporates relatively rapidly, leaving behind a nanofilm consisting mostly of PEG and surfactant. Due to surface tension, this nanofilm rises in the form of a meniscus around any particles that are sitting on the substrate and embedded in the film (118). The lensless sensing detection limit is again ~100 nm (119), similar to the tilting-based approach in terms of both limit of detection and field of view. However, in this approach, no particles are lost, as may happen when the excess liquid is removed via tilting. The physical nature of the nanolenses is also different in this approach in that the lenses are part of a continuous film coating, as opposed to isolated droplets.

The final approach to nanolens formation involves the condensation of a nanofilm from a vapor. One advantage of this technique is that particles can be initially deposited on the substrate via multiple means; they do not need to be first suspended in the same liquid that will form the nanolenses. This makes the condensation approach more compatible with particles having various forms of surface chemistry. After particle deposition, a continuous nanofilm of pure PEG is condensed on the substrate, and nanolenses form around the particles due to surface tension (**Figure 8*e***). Another advantage of this technique is that it enables direct control over the thickness of the film that is formed. This control allows the size of the nanolens to be tuned to achieve the maximum possible signal, which has enabled the limit of detection to be reduced to ~40 nm (**Figure 8*f***) (120). Furthermore, the optimum signal for each particle correlates strongly with the particle's size. By using image processing routines to extract the optimum signal for each particle, an automated sensor platform has been able to measure particle-size distributions within the sample (**Figure 8*g,b***). As such, the platform can be considered an alternative to dynamic light scattering (122, 123), nanoparticle tracking analysis (124), or electron microscopy for nanoparticle sizing. Additionally, this entire approach has been integrated into a compact, cost-effective, field-portable platform (weighing <500 g), taking advantage of the benefits of the lensfree on-chip imaging approach (**Figure 8*g***).

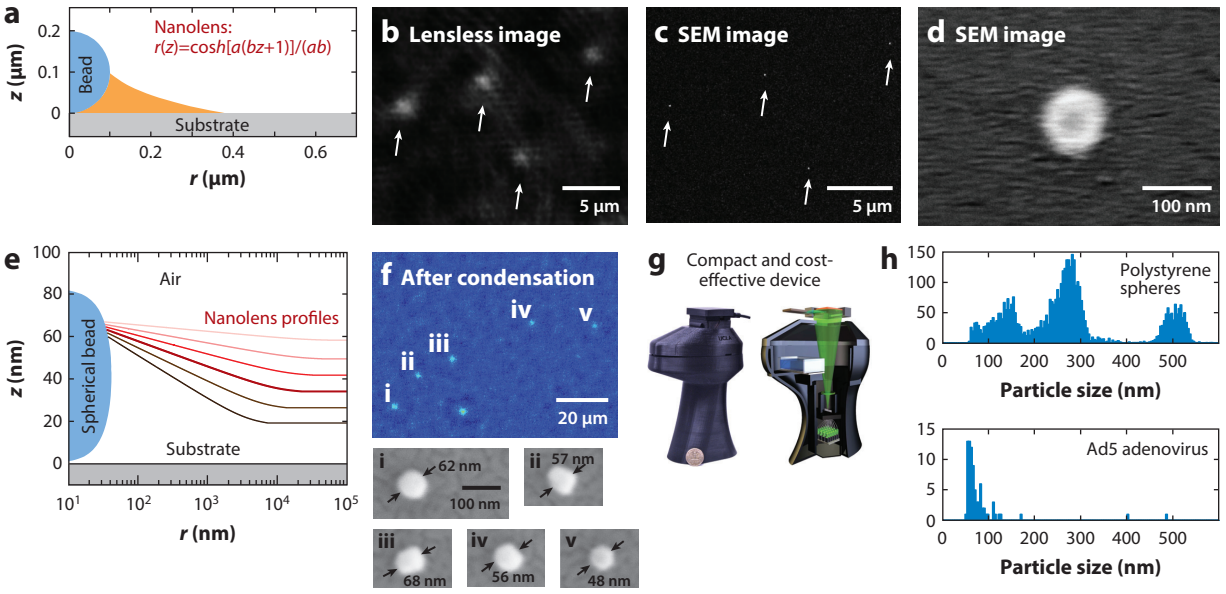

Figure 8

Nanoparticle and virus sensing using self-assembled nanolenses. (*a*) Isolated nanolens geometry formed in the wake of a receding droplet. (*b*) Individual adenoviruses imaged using lensless phase reconstruction with isolated nanolenses. (*c*) Scanning electron microscope (SEM) image of the same viruses used for verification. (*d*) High-magnification SEM image of a single adenovirus. (*e*) Continuous-film nanolens geometry formed via vapor condensation. (*f*) A phase image of individual polystyrene nanobeads made visible with continuous-film nanolenses. SEM verification images are shown below the lensless image. (*g*) (*Left*) Photograph and (*right*) computer graphic diagram of a compact device for in situ nanolens formation and lensless imaging. (*h*) Example particle-sizing histograms obtained using the device in panel *g*. Panels *a–d* modified from Reference 117. Panels *e* and *f* modified from Reference 120. Panels *g* and *h* modified from Reference 121.

3.2. Cell Capture, Manipulation, and Sensing

Many applications of lensless imaging involve the detection and monitoring of cells. Specialized substrates that enable the capture or manipulation of cells can aid in this task and provide extra functionality. One example is the use of a perforated transparent substrate that can be used to trap, for instance, HeLa cells through the use of an applied negative pressure. The number of trapped cells can then be counted using a lensless imaging setup (125). Similarly, small microwells can be used to trap individual cells (126). For selectivity, microarrays of antibodies can be used to capture specific cells for quantification (40). In another example, the active capture surface is integrated directly into the fabrication of the image sensor (51). Finally, a photoconductive substrate material can be used in an optoelectronic tweezer setup; when combined with lensless imaging, this approach enables real-time manipulation of a large number of cells across the entire active area of the image sensor (>20 mm^2) (127).

3.3. Bead-Based Labeling for Specific Sensing and Cytometric Analysis in a Lensless Design

Specificity is extremely important for any type of biochemical sensor. Often, fluorescent molecules are used as labels that can be bound to specific biomolecules to show their presence and location. However, fluorescent labels are unsuitable for a high-resolution lensless holographic imaging setup

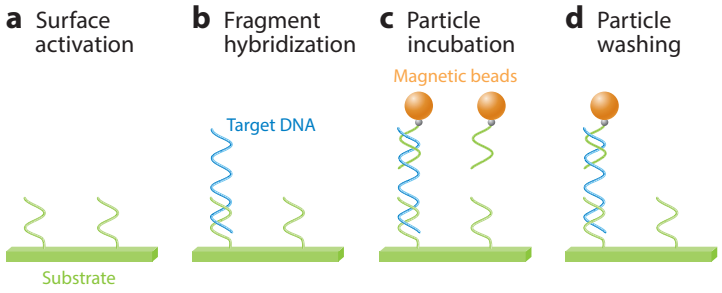

Figure 9

DNA sensing using magnetic beads as labels. This sandwich assay enables the detection of individual strands of DNA in a lensless imaging system. (*a*) The substrate is functionalized with DNA complementary to part of the target DNA. (*b*) Target DNA binds to the functionalized surface. (*c*) Magnetic beads functionalized with complementary DNA bind to the free portion of the captured target DNA strand. (*d*) Unbound beads are washed away, and the remaining beads indicate the presence of individual target strands. Modified from Reference 129.

because their emission is incoherent with their excitation. Instead, beads with biomolecularly functionalized surfaces can be used to provide specificity, as the scattering from these beads is coherent with their illumination. Metallic beads work especially well due to their strong scattering properties, which can be enhanced even further by taking advantage of their plasmonic resonances.

Gold and silver nanobeads have been used as specific labels to identify and count the number of CD4 and CD8 cells in a cell suspension (128). CD4 and CD8 cells are specific types of T lymphocytes, and their relative populations are important for evaluating the stage of human immunodeficiency virus (HIV) infection or AIDS, as well as for evaluating the efficacy of antiretroviral treatment. Counting the relative populations of these cells can be challenging, however, because the only significant difference between these cells is in the types of proteins expressed on their membranes. Under a microscope, both types of cells look virtually identical. In order to sense and count these cells in a lensless imaging setup, the authors of this study (128) used gold nanoparticles functionalized with anti-CD4 antibodies and silver nanoparticles functionalized with anti-CD8 as labels. After incubation of the cells with the nanoparticles, the CD4 cells became coated with gold nanoparticles and the CD8 cells became coated with silver nanoparticles. By comparing the spectral response of different cells under lensless imaging, the investigators were able to discriminate these two types of cells with greater than 95% accuracy using a machine learning algorithm.

Beads have also been used as labels for sensing DNA in a sandwich assay that is read out using lensless imaging (129). In this technique (**Figure 9**), a substrate is first functionalized with short strands of DNA that are complementary to the bases near one end of the target DNA sequence. Magnetic beads are also functionalized with short strands of DNA that are complementary to the bases at the other end of the target DNA sequence. First, a sample to be analyzed is incubated with the substrate; then, the substrate is incubated with the functionalized magnetic beads. If the target strands were present in the sample, they will be labeled with magnetic beads. These magnetic beads are then quantified using a lensfree imaging system. Another sandwich-type assay using beads has also been read out using a lensless system, although in this case, bead and fluid motion for the incubation and washing steps was controlled by surface acoustic wave transducers (130).

3.4. Lensless Plasmonic Sensing

Lensless imaging can be combined with plasmonically active substrates for sensing purposes (131). In one application, transmission through a plasmonic nanohole array was monitored using a

portable sensing apparatus (132, 133). Arrays of nanoscale holes in thin metal films had previously been observed to exhibit extraordinary optical transmission (134, 135); that is, the transmission through the array exceeded the predicted transmission through a single hole times the number of holes. This phenomenon occurs because the transmission is enhanced via surface plasmon waves propagating along the film. This extraordinary optical transmission exhibits a strong resonance peak at a specific wavelength. The resonance is quite sensitive to the refractive index of the material within the evanescent field of the nanohole array. If the nanohole array is biochemically functionalized to capture specific biomolecules, it can then act as a sensor through monitoring of the shift of the resonance peak. If the nanohole array is initially illuminated by a wavelength tuned to the resonance corresponding to no bound biomolecules, then when biomolecules start to bind to the sensor, a drop in transmission occurs, and this drop can be observed with a lensless imaging system (131, 132). In such a device, many plasmonic arrays functionalized for different analytes can be used in parallel to develop a massively multiplexed sensor. For improved sensitivity, two wavelengths can be used simultaneously: one tuned to the initial resonance and one tuned slightly in the direction the resonance will shift. The transmission ratio between the two wavelengths can be used to measure the degree of binding of the analyte with a sensitivity approximately a factor of two higher than that of the single-LED device (133). These and similar systems have been used to sense biomolecules (132, 133).

4. FUTURE OUTLOOK

Although lensless imaging has already demonstrated significant results in terms of its ability to capture large-field-of-view images with high resolution and image quality in a compact and cost-effective platform, there are still a number of areas for future improvement. One such area is that of resolution. Investigators have obtained a resolution equivalent to that from 1.4-NA microscope objectives (see Section 2.6), which is approximately as high as can be achieved using standard objective lenses. Yet this need not pose a hard limit for lensless imaging because, due to the computational imaging approach, resolution is more closely tied to SNR than to any of the physical parameters of the system. Through higher-SNR systems and new algorithms capable of extrapolating high–spatial frequency information from low-frequency knowledge of the complete field (e.g., through analytic continuation), it should be possible to further enhance resolution, with the assumption that a high index medium (e.g., an oil) fills in the space between the sample and sensor planes.

Complementary to resolution is sensitivity. Current lensless on-chip imaging approaches have a sensitivity limit of ~250 nm without nanolenses, and ~40 nm using self-assembled nanolenses. With future improvements to imaging SNR, as well as potential improvements to sample preparation and nanolens formation, it should be possible to reduce both of these limits.

Another area of improvement is that of imaging speed. Approaches such as the pixel super-resolution discussed in Section 2.4 and the multiheight phase recovery discussed in Section 2.6 require the capture of many images in sequence, which can limit their application in systems with rapid dynamics. The use of high-speed image sensors with bright light sources can solve this deficiency. In addition to the speed of image acquisition, the duration of image processing and computational reconstruction steps can sometimes pose a challenge in certain applications. These speeds can be improved through distributed graphical processing unit (GPU) implementation; in fact, this has already been done for some applications (91). Additionally, the development of algorithms that provide a similar quality of results with fewer raw images or fewer computational steps or iterations will help speed processing and image reconstruction. An example is the use of the transport-of-intensity equation, as discussed in Section 2.6.

Finally, there is still a significant opportunity for the distribution of this technology in point-of-care or low-resource settings. Biomedical diagnostics in these areas form one of the primary motivations for the development of these compact, portable, and cost-effective lensless imaging and cytometry approaches. Although some field tests of lensless on-chip imaging have already been performed, much more work is required to test and evaluate these devices in the situations and settings that motivated them. Undoubtedly, this testing will reveal new areas for improvement that can be incorporated into later generations of lensless imaging, diagnostics, and cytometry devices.

DISCLOSURE STATEMENT

A.O. is the founder of a company, Holomic LLC, that commercializes computational imaging, sensing, and diagnostics technologies. A.O. and E.M. are coinventors of issued and pending patents on lensfree imaging and sensing techniques.

LITERATURE CITED

1. Hooke R. 1665. *Micrographia*. London: R. Soc.
2. Vashist SK, Mudanyali O, Schneider EM, Zengerle R, Ozcan A. 2013. Cellphone-based devices for bioanalytical sciences. *Anal. Bioanal. Chem.* 406:3263–77
3. Ozcan A. 2014. Mobile phones democratize and cultivate next-generation imaging, diagnostics and measurement tools. *Lab Chip* 14:3187–94
4. Greenbaum A, Ozcan A. 2012. Maskless imaging of dense samples using pixel super-resolution based multi-height lensfree on-chip microscopy. *Opt. Expr.* 20:3129–43
5. Greenbaum A, Sikora U, Ozcan A. 2012. Field-portable wide-field microscopy of dense samples using multi-height pixel super-resolution based lensfree imaging. *Lab Chip* 12:1242–45
6. Greenbaum A, Feizi A, Akbari N, Ozcan A. 2013. Wide-field computational color imaging using pixel super-resolved on-chip microscopy. *Opt. Expr.* 21:12469–83
7. Greenbaum A, Akbari N, Feizi A, Luo W, Ozcan A. 2013. Field-portable pixel super-resolution colour microscope. *PLOS ONE* 8:e76475
8. Bishara W, Sikora U, Mudanyali O, Su T-W, Yaglidere O, et al. 2011. Holographic pixel super-resolution in portable lensless on-chip microscopy using a fiber-optic array. *Lab Chip* 11:1276–79
9. Bishara W, Sikora U, Mudanyali O, Su T-W, Yaglidere O, et al. 2011. Handheld, lensless microscope identifies malaria parasites. *SPIE Newsroom*, Aug. 5. **http://spie.org/x51571.xml**
10. Su T-W, Xue L, Ozcan A. 2012. High-throughput lensfree 3D tracking of human sperms reveals rare statistics of helical trajectories. *PNAS* 109:16018–22
11. Su T-W, Choi I, Feng J, Huang K, McLeod E, Ozcan A. 2013. Sperm trajectories form chiral ribbons. *Sci. Rep.* 3:1664
12. Seo S, Isikman SO, Sencan I, Mudanyali O, Su T-W, et al. 2010. High-throughput lens-free blood analysis on a chip. *Anal. Chem.* 82:4621–27
13. Arpali SA, Arpali C, Coskun AF, Chiang H-H, Ozcan A. 2012. High-throughput screening of large volumes of whole blood using structured illumination and fluorescent on-chip imaging. *Lab Chip* 12:4968–71
14. Tseng D, Mudanyali O, Oztoprak C, Isikman SO, Sencan I, et al. 2010. Lensfree microscopy on a cellphone. *Lab Chip* 10:1787–92
15. Navruz I, Coskun AF, Wong J, Mohammad S, Tseng D, et al. 2013. Smart-phone based computational microscopy using multi-frame contact imaging on a fiber-optic array. *Lab Chip* 13:4015–23
16. Zhu H, Yaglidere O, Su T-W, Tseng D, Ozcan A. 2011. Cost-effective and compact wide-field fluorescent imaging on a cell-phone. *Lab Chip* 11:315–22
17. Zhu H, Sencan I, Wong J, Dimitrov S, Tseng D, et al. 2013. Cost-effective and rapid blood analysis on a cell-phone. *Lab Chip* 13:1282–88

18. Mudanyali O, Dimitrov S, Sikora U, Padmanabhan S, Navruz I, Ozcan A. 2012. Integrated rapid-diagnostic-test reader platform on a cellphone. *Lab Chip* 12:2678–86
19. Coskun AF, Nagi R, Sadeghi K, Phillips S, Ozcan A. 2013. Albumin testing in urine using a smart-phone. *Lab Chip* 13:4231–38
20. Wei Q, Qi H, Luo W, Tseng D, Ki SJ, et al. 2013. Fluorescent imaging of single nanoparticles and viruses on a smart phone. *ACS Nano* 7:9147–55
21. Ludwig SKJ, Zhu H, Phillips S, Shiledar A, Feng S, et al. 2014. Cellphone-based detection platform for RBST biomarker analysis in milk extracts using a microsphere fluorescence immunoassay. *Anal. Bioanal. Chem.* 406:6857–66
22. Wei Q, Luo W, Chiang S, Kappel T, Mejia C, et al. 2014. Imaging and sizing of single DNA molecules on a mobile phone. *ACS Nano* 8:12725–33
23. Koydemir HC, Göröcs Z, Tseng D, Cortazar B, Feng S, et al. 2015. Rapid imaging, detection and quantification of *Giardia lamblia* cysts using mobile-phone based fluorescent microscopy and machine learning. *Lab Chip* 15:1284–93
24. Berg B, Cortazar B, Tseng D, Ozkan H, Feng S, et al. 2015. Cellphone-based hand-held microplate reader for point-of-care testing of enzyme-linked immunosorbent assays. *ACS Nano* 9: 7857–66
25. Cybulski JS, Clements J, Prakash M. 2014. Foldscope: origami-based paper microscope. *PLOS ONE* 9:e98781
26. Breslauer DN, Maamari RN, Switz NA, Lam WA, Fletcher DA. 2009. Mobile phone based clinical microscopy for global health applications. *PLOS ONE* 4:e6320
27. D'Ambrosio MV, Bakalar M, Bennuru S, Reber C, Skandarajah A, et al. 2015. Point-of-care quantification of blood-borne filarial parasites with a mobile phone microscope. *Sci. Transl. Med.* 7:286re4
28. Maamari RN, Ausayakhun S, Margolis TP, Fletcher DA, Keenan JD. 2014. Novel telemedicine device for diagnosis of corneal abrasions and ulcers in resource-poor settings. *JAMA Ophthalmol.* 132:894–95
29. Switz NA, D'Ambrosio MV, Fletcher DA. 2014. Low-cost mobile phone microscopy with a reversed mobile phone camera lens. *PLOS ONE* 9:e95330
30. Maamari RN, Keenan JD, Fletcher DA, Margolis TP. 2014. A mobile phone–based retinal camera for portable wide field imaging. *Br. J. Ophthalmol.* 98:438–41
31. Lee S, Oncescu V, Mancuso M, Mehta S, Erickson D. 2014. A smartphone platform for the quantification of vitamin D levels. *Lab Chip* 14:1437–42
32. Jiang L, Mancuso M, Lu Z, Akar G, Cesarman E, Erickson D. 2014. Solar thermal polymerase chain reaction for smartphone-assisted molecular diagnostics. *Sci. Rep.* 4:4137
33. Oncescu V, Mancuso M, Erickson D. 2014. Cholesterol testing on a smartphone. *Lab Chip* 14:759–63
34. Oncescu V, O'Dell D, Erickson D. 2013. Smartphone based health accessory for colorimetric detection of biomarkers in sweat and saliva. *Lab Chip* 13:3232–38
35. McLeod E, Wei Q, Ozcan A. 2015. Democratization of nanoscale imaging and sensing tools using photonics. *Anal. Chem.* 87:6434–45
36. Ozcan A, Demirci U. 2007. Ultra wide-field lens-free monitoring of cells on-chip. *Lab Chip* 8:98–106
37. Seo S, Su T-W, Tseng DK, Erlinger A, Ozcan A. 2009. Lensfree holographic imaging for on-chip cytometry and diagnostics. *Lab Chip* 9:777–87
38. Goodman JW. 2000. *Statistical Optics*. New York: Wiley. 572 pp. 1st ed.
39. Su T-W, Seo S, Erlinger A, Ozcan A. 2009. High-throughput lensfree imaging and characterization of a heterogeneous cell solution on a chip. *Biotechnol. Bioeng.* 102:856–68
40. Stybayeva G, Mudanyali O, Seo S, Silangcruz J, Macal M, et al. 2010. Lensfree holographic imaging of antibody microarrays for high-throughput detection of leukocyte numbers and function. *Anal. Chem.* 82:3736–44
41. Tanaka T, Saeki T, Sunaga Y, Matsunaga T. 2010. High-content analysis of single cells directly assembled on CMOS sensor based on color imaging. *Biosens. Bioelectron.* 26:1460–65
42. Zhang X, Khimji I, Gurkan UA, Safaee H, Catalano PN, et al. 2011. Lensless imaging for simultaneous microfluidic sperm monitoring and sorting. *Lab Chip* 11:2535–40
43. Moscelli N, van den Driesche S, Witarski W, Pastorekova S, Vellekoop MJ. 2011. An imaging system for real-time monitoring of adherently grown cells. *Sens. Actuators A* 172:175–80

44. Kim SB, Bae H, Cha JM, Moon SJ, Dokmeci MR, et al. 2011. A cell-based biosensor for real-time detection of cardiotoxicity using lensfree imaging. *Lab Chip* 11:1801–7
45. Jin G, Yoo I-H, Pack SP, Yang J-W, Ha U-H, et al. 2012. Lens-free shadow image based high-throughput continuous cell monitoring technique. *Biosens. Bioelectron.* 38:126–31
46. Dolega ME, Allier C, Kesavan SV, Gerbaud S, Kermarrec F, et al. 2013. Label-free analysis of prostate acini-like 3D structures by lensfree imaging. *Biosens. Bioelectron.* 49:176–83
47. Kesavan SV, Momey F, Cioni O, David-Watine B, Dubrulle N, et al. 2014. High-throughput monitoring of major cell functions by means of lensfree video microscopy. *Sci. Rep.* 4:5942
48. Kwak YH, Lee J, Lee J, Kwak SH, Oh S, et al. 2014. A simple and low-cost biofilm quantification method using LED and CMOS image sensor. *J. Microbiol. Methods* 107:150–56
49. Penwill LA, Batten GE, Castagnetti S, Shaw AM. 2014. Growth phenotype screening of *Schizosaccharomyces pombe* using a lensless microscope. *Biosens. Bioelectron.* 54:345–50
50. Pushkarsky I, Liu Y, Weaver W, Su T-W, Mudanyali O, et al. 2014. Automated single-cell motility analysis on a chip using lensfree microscopy. *Sci. Rep.* 4:4717
51. Musayev J, Altiner C, Adiguzel Y, Kulah H, Eminoglu S, Akin T. 2014. Capturing and detection of MCF-7 breast cancer cells with a CMOS image sensor. *Sens. Actuators A* 215:105–14
52. Roy M, Seo D, Oh C-H, Nam M-H, Kim YJ, Seo S. 2015. Low-cost telemedicine device performing cell and particle size measurement based on lens-free shadow imaging technology. *Biosens. Bioelectron.* 67:715–23
53. Tsai H-F, Tsai Y-C, Yagur-Kroll S, Palevsky N, Belkin S, Cheng J-Y. 2015. Water pollutant monitoring by a whole cell array through lens-free detection on CCD. *Lab Chip* 15:1472–80
54. Kesavan SV, Navarro FP, Menneteau M, Mittler F, David-Watine B, et al. 2014. Real-time label-free detection of dividing cells by means of lensfree video-microscopy. *J. Biomed. Opt.* 19:036004
55. Cui X, Lee LM, Heng X, Zhong W, Sternberg PW, et al. 2008. Lensless high-resolution on-chip optofluidic microscopes for *Caenorhabditis elegans* and cell imaging. *PNAS* 105:10670–75
56. Lee LM, Cui X, Yang C. 2009. The application of on-chip optofluidic microscopy for imaging *Giardia lamblia* trophozoites and cysts. *Biomed. Microdevices* 11:951–58
57. Coskun AF, Su T-W, Ozcan A. 2010. Wide field-of-view lens-free fluorescent imaging on a chip. *Lab Chip* 10:824–27
58. Coskun AF, Sencan I, Su T-W, Ozcan A. 2010. Lensless wide-field fluorescent imaging on a chip using compressive decoding of sparse objects. *Opt. Expr.* 18:10510–23
59. Shanmugam A, Salthouse C. 2014. Lensless fluorescence imaging with height calculation. *J. Biomed. Opt.* 19:016002
60. Coskun AF, Sencan I, Su T-W, Ozcan A. 2011. Wide-field lensless fluorescent microscopy using a tapered fiber-optic faceplate on a chip. *Analyst* 136:3512–18
61. Martinelli L, Choumane H, Ha K-N, Sagarzazu G, Goutel C, et al. 2007. Sensor-integrated fluorescent microarray for ultrahigh sensitivity direct-imaging bioassays: role of a high rejection of excitation light. *Appl. Phys. Lett.* 91:083901
62. Ah Lee S, Ou X, Lee JE, Yang C. 2013. Chip-scale fluorescence microscope based on a silo-filter complementary metal-oxide semiconductor image sensor. *Opt. Lett.* 38:1817–19
63. Coskun AF, Sencan I, Su T-W, Ozcan A. 2011. Lensfree fluorescent on-chip imaging of transgenic *Caenorhabditis elegans* over an ultra-wide field-of-view. *PLOS ONE* 6:e15955
64. Khademhosseinieh B, Sencan I, Biener G, Su T-W, Coskun AF, et al. 2010. Lensfree on-chip imaging using nanostructured surfaces. *Appl. Phys. Lett.* 96:171106
65. Khademhosseinieh B, Biener G, Sencan I, Ozcan A. 2010. Lensfree color imaging on a nanostructured chip using compressive decoding. *Appl. Phys. Lett.* 97:211112
66. Han C, Pang S, Bower DV, Yiu P, Yang C. 2013. Wide field-of-view on-chip Talbot fluorescence microscopy for longitudinal cell culture monitoring from within the incubator. *Anal. Chem.* 85:2356–60
67. Richardson WH. 1972. Bayesian-based iterative method of image restoration. *J. Opt. Soc. Am.* 62:55–59
68. Lucy LB. 1974. An iterative technique for the rectification of observed distributions. *Astron. J.* 79:745
69. Sencan I, Coskun AF, Sikora U, Ozcan A. 2014. Spectral demultiplexing in holographic and fluorescent on-chip microscopy. *Sci. Rep.* 4:3760

70. Gabor D. 1948. A new microscopic principle. *Nature* 161:777–78
71. Göröcs Z, Ozcan A. 2013. On-chip biomedical imaging. *Biomed. Eng. IEEE Rev.* 6:29–46
72. Goodman J. 2004. *Introduction to Fourier Optics*. Greenwood Village, CO: Roberts. 491 pp. 3rd ed.
73. Mudanyali O, Tseng D, Oh C, Isikman SO, Sencan I, et al. 2010. Compact, light-weight and cost-effective microscope based on lensless incoherent holography for telemedicine applications. *Lab Chip* 10:1417–28
74. Ozcan A. 2005. *Non-destructive characterization tools based on spectral interferometry and minimum phase functions*. PhD thesis, Dep. Electr. Eng., Stanford Univ., Stanford, CA
75. Papoulis A. 1975. A new algorithm in spectral analysis and band-limited extrapolation. *IEEE Trans. Circuits Syst.* 22:735–42
76. Repetto L, Piano E, Pontiggia C. 2004. Lensless digital holographic microscope with light-emitting diode illumination. *Opt. Lett.* 29:1132–34
77. Hardie RC. 1998. High-resolution image reconstruction from a sequence of rotated and translated frames and its application to an infrared imaging system. *Opt. Eng.* 37:247–60
78. Barron JL, Fleet DJ, Beauchemin SS, Burkitt TA. 1992. Performance of optical flow techniques. *Int. J. Comput. Vis.* 12:43–77
79. Elad M, Hel-Or Y. 2001. A fast super-resolution reconstruction algorithm for pure translational motion and common space-invariant blur. *IEEE Trans. Image Process.* 10:1187–93
80. Bishara W, Su T-W, Coskun AF, Ozcan A. 2010. Lensfree on-chip microscopy over a wide field-of-view using pixel super-resolution. *Opt. Expr.* 18:11181–91
81. Bishara W, Zhu H, Ozcan A. 2010. Holographic opto-fluidic microscopy. *Opt. Expr.* 18:27499–510
82. Greenbaum A, Luo W, Khademhosseinieh B, Su T-W, Coskun AF, Ozcan A. 2013. Increased space-bandwidth product in pixel super-resolved lensfree on-chip microscopy. *Sci. Rep.* 3:1717
83. McLeod E, Luo W, Mudanyali O, Greenbaum A, Ozcan A. 2013. Toward giga-pixel nanoscopy on a chip: a computational wide-field look at the nano-scale without the use of lenses. *Lab Chip* 13:2028–35
84. Greenbaum A, Luo W, Su T-W, Göröcs Z, Xue L, et al. 2012. Imaging without lenses: achievements and remaining challenges of wide-field on-chip microscopy. *Nat. Methods* 9:889–95
85. Zheng G, Lee SA, Yang S, Yang C. 2010. Sub-pixel resolving optofluidic microscope for on-chip cell imaging. *Lab Chip* 10:3125–29
86. Huang X, Guo J, Wang X, Yan M, Kang Y, Yu H. 2014. A contact-imaging based microfluidic cytometer with machine-learning for single-frame super-resolution processing. *PLOS ONE* 9:e104539
87. Zheng G, Lee SA, Antebi Y, Elowitz MB, Yang C. 2011. The ePetri dish, an on-chip cell imaging platform based on subpixel perspective sweeping microscopy (SPSM). *PNAS* 108:16889–94
88. Lee SA, Zheng G, Mukherjee N, Yang C. 2012. On-chip continuous monitoring of motile microorganisms on an ePetri platform. *Lab Chip* 12:2385–90
89. Han C, Yang C. 2014. Viral plaque analysis on a wide field-of-view, time-lapse, on-chip imaging platform. *Analyst* 139:3727–34
90. Lee SA, Erath J, Zheng G, Ou X, Willems P, et al. 2014. Imaging and identification of waterborne parasites using a chip-scale microscope. *PLOS ONE* 9:e89712
91. Isikman SO, Bishara W, Mavandadi S, Yu FW, Feng S, et al. 2011. Lens-free optical tomographic microscope with a large imaging volume on a chip. *PNAS* 108:7296–301
92. Isikman SO, Bishara W, Ozcan A. 2011. Partially coherent lensfree tomographic microscopy. *Appl. Opt.* 50:H253–64
93. Meng H, Hussain F. 1995. In-line recording and off-axis viewing technique for holographic particle velocimetry. *Appl. Opt.* 34:1827–40
94. Su T-W, Isikman SO, Bishara W, Tseng D, Erlinger A, Ozcan A. 2010. Multi-angle lensless digital holography for depth resolved imaging on a chip. *Opt. Expr.* 18:9690–711
95. Brooks RA, Di Chiro G. 1975. Theory of image reconstruction in computed tomography. *Radiology* 117:561–72
96. Isikman SO, Bishara W, Sikora U, Yaglidere O, Yeah J, Ozcan A. 2011. Field-portable lensfree tomographic microscope. *Lab Chip* 11:2222–30
97. Isikman SO, Greenbaum A, Luo W, Coskun AF, Ozcan A. 2012. Giga-pixel lensfree holographic microscopy and tomography using color image sensors. *PLOS ONE* 7:e45044

98. Isikman SO, Bishara W, Zhu H, Ozcan A. 2011. Optofluidic tomography on a chip. *Appl. Phys. Lett.* 98:161109
99. Greenbaum A, Zhang Y, Feizi A, Chung P-L, Luo W, et al. 2014. Wide-field computational imaging of pathology slides using lens-free on-chip microscopy. *Sci. Transl. Med.* 6:267ra175
100. Biener G, Greenbaum A, Isikman SO, Lee K, Tseng D, Ozcan A. 2011. Combined reflection and transmission microscope for telemedicine applications in field settings. *Lab Chip.* 11:2738–43
101. Gerchberg R, Saxton O. 1972. A practical algorithm for the determination of the phase from image and diffraction plane pictures. *Optik* 35:237–46
102. Fienup JR. 1982. Phase retrieval algorithms: a comparison. *Appl. Opt.* 21:2758–69
103. Weidling J, Isikman SO, Greenbaum A, Ozcan A, Botvinick E. 2012. Lens-free computational imaging of capillary morphogenesis within three-dimensional substrates. *J. Biomed. Opt.* 17:126018
104. Teague MR. 1983. Deterministic phase retrieval: a Green's function solution. *J. Opt. Soc. Am.* 73:1434–41
105. Waller L, Tian L, Barbastathis G. 2010. Transport of intensity imaging with higher order derivatives. *Opt. Expr.* 18:12552–61
106. Luo W, Greenbaum A, Zhang Y, Ozcan A. 2015. Synthetic aperture-based on-chip microscopy. *Light Sci. Appl.* 4:e261
107. Göröcs Z, Orzó L, Kiss M, Tóth V, Tőkés S. 2010. In-line color digital holographic microscope for water quality measurements. *Proc. SPIE* 7376:737614
108. Dijkstra EW. 1959. A note on two problems in connexion with graphs. *Numer. Math.* 1:269–71
109. Kim D-S, Choi J-H, Nam M-H, Yang J-W, Pak JJ, Seo S. 2011. LED and CMOS image sensor based hemoglobin concentration measurement technique. *Sens. Actuators B* 157:103–9
110. Lee J, Kwak YH, Paek S-H, Han S, Seo S. 2014. CMOS image sensor–based ELISA detector using lens-free shadow imaging platform. *Sens. Actuators B* 196:511–17
111. Pang S, Cui X, DeModena J, Wang YM, Sternberg P, Yang C. 2010. Implementation of a color-capable optofluidic microscope on a RGB CMOS color sensor chip substrate. *Lab Chip* 10:411–14
112. Lee SA, Leitao R, Zheng G, Yang S, Rodriguez A, Yang C. 2011. Color capable sub-pixel resolving optofluidic microscope and its application to blood cell imaging for malaria diagnosis. *PLOS ONE* 6:e26127
113. Isikman SO, Sencan I, Mudanyali O, Bishara W, Oztoprak C, Ozcan A. 2010. Color and monochrome lensless on-chip imaging of *Caenorhabditis elegans* over a wide field-of-view. *Lab Chip* 10:1109–12
114. Arlett JL, Myers EB, Roukes ML. 2011. Comparative advantages of mechanical biosensors. *Nat. Nanotechnol.* 6:203–15
115. Su J, Goldberg AFG, Stoltz BM. 2016. Label-free detection of single nanoparticles and biological molecules using microtoroid optical resonators. *Light Sci. Appl.* 5:e16001
116. Mudanyali O, Bishara W, Ozcan A. 2011. Lensfree super-resolution holographic microscopy using wetting films on a chip. *Opt. Expr.* 19:17378–89
117. Mudanyali O, McLeod E, Luo W, Greenbaum A, Coskun AF, et al. 2013. Wide-field optical detection of nanoparticles using on-chip microscopy and self-assembled nanolenses. *Nat. Photonics* 7:247–54
118. Allier CP, Hiernard G, Poher V, Dinten JM. 2010. Bacteria detection with thin wetting film lensless imaging. *Biomed. Opt. Expr.* 1:762–70
119. Hennequin Y, Allier CP, McLeod E, Mudanyali O, Migliozzi D, et al. 2013. Optical detection and sizing of single nanoparticles using continuous wetting films. *ACS Nano* 7:7601–9
120. McLeod E, Nguyen C, Huang P, Luo W, Veli M, Ozcan A. 2014. Tunable vapor-condensed nanolenses. *ACS Nano* 8:7340–49
121. McLeod E, Dincer TU, Veli M, Ertas YN, Nguyen C, et al. 2015. High-throughput and label-free single nanoparticle sizing based on time-resolved on-chip microscopy. *ACS Nano* 9:3265–73
122. Berne BJ, Pecora R. 2000. *Dynamic Light Scattering: With Applications to Chemistry, Biology, and Physics*. Mineola, NY: Courier Dover. 388 pp.
123. Filella M, Zhang J, Newman ME, Buffle J. 1997. Analytical applications of photon correlation spectroscopy for size distribution measurements of natural colloidal suspensions: capabilities and limitations. *Colloids Surf. A* 120:27–46
124. Filipe V, Hawe A, Jiskoot W. 2010. Critical evaluation of nanoparticle tracking analysis (NTA) by nanosight for the measurement of nanoparticles and protein aggregates. *Pharm. Res.* 27:796–810

125. Saeki T, Hosokawa M, Lim T, Harada M, Matsunaga T, Tanaka T. 2014. Digital cell counting device integrated with a single-cell array. *PLOS ONE* 9:e89011
126. Tanaka T, Sunaga Y, Hatakeyama K, Matsunaga T. 2010. Single-cell detection using a thin film transistor photosensor with micro-partitions. *Lab Chip* 10:3348–54
127. Huang K-W, Su T-W, Ozcan A, Chiou P-Y. 2013. Optoelectronic tweezers integrated with lensfree holographic microscopy for wide-field interactive cell and particle manipulation on a chip. *Lab Chip* 13:2278–84
128. Wei Q, McLeod E, Qi H, Wan Z, Sun R, Ozcan A. 2013. On-chip cytometry using plasmonic nanoparticle enhanced lensfree holography. *Sci. Rep.* 3:1699
129. Colle F, Vercruysse D, Peeters S, Liu C, Stakenborg T, et al. 2013. Lens-free imaging of magnetic particles in DNA assays. *Lab Chip* 13:4257–62
130. Bourquin Y, Reboud J, Wilson R, Zhang Y, Cooper JM. 2011. Integrated immunoassay using tuneable surface acoustic waves and lensfree detection. *Lab Chip* 11:2725–30
131. Khademhosseinieh B, Biener G, Sencan I, Su T-W, Coskun AF, Ozcan A. 2010. Lensfree sensing on a microfluidic chip using plasmonic nanoapertures. *Appl. Phys. Lett.* 97:221107
132. Cetin AE, Coskun AF, Galarreta BC, Huang M, Herman D, et al. 2014. Handheld high-throughput plasmonic biosensor using computational on-chip imaging. *Light Sci. Appl.* 3:e122
133. Coskun AF, Cetin AE, Galarreta BC, Alvarez DA, Altug H, Ozcan A. 2014. Lensfree optofluidic plasmonic sensor for real-time and label-free monitoring of molecular binding events over a wide field-of-view. *Sci. Rep.* 4:6789
134. Ebbesen TW, Lezec HJ, Ghaemi HF, Thio T, Wolff PA. 1998. Extraordinary optical transmission through sub-wavelength hole arrays. *Nature* 391:667–69
135. Rindzevicius T, Alaverdyan Y, Dahlin A, Höök F, Sutherland DS, Käll M. 2005. Plasmonic sensing characteristics of single nanometric holes. *Nano Lett.* 5:2335–39